Earth System
The First ~~Hillslope Therm~~ ~~arst~~ Invertory for the Permafrost Region of the Qilian Mountains

Xiaoqing Peng[1,3], Guangshang Yang[1], Oliver W. Frauenfeld[2], Xuanjia Li[1], Weiwei Tian[1], Guanqun Chen[1], Yuan Huang[1], Gang Wei[1], Jing Luo[4], Cuicui Mu[1,3], Fujun Niu[4]

[1]Key Laboratory of Western China's Environmental Systems (Ministry of Education), College of Earth and Environmental Sciences, Lanzhou University, Lanzhou, 730000, China

[2]Department of Geography, Texas A&M University, College Station, TX 77843-3147, USA

[3]Observation and Research Station on Eco-Environment of Frozen Ground in the Qilian Mountains, Lanzhou University, Lanzhou 730000, China

[4]State Key Laboratory of Frozen Soil Engineering, Northwest Institute of Eco-Environment and Resources, Chinese Academy of Sciences, Lanzhou 730000, China

* Corresponding author: Guangshang Yang (220220948511@lzu.edu.cn)

Abstract:

Climate warming and anthropogenic disturbances result in permafrost degradation in cold regions, including in the Qilian Mountains. These changes lead to extensive hillslope thermokarst (HT) formation, such as retrogressive thaw slumps, active-layer detachment slides, and thermal erosion gullies. These in turn cause, e.g., degradation of local vegetation, economic losses, infrastructure damages, and threats to human safety. However, despite its importance, there is currently no thermokarst inventory for the Qilian Mountains. Through manual visual interpretation and field validation, we therefore produce the first quantification of HT features. We count a total of 1064 HT features, with 67% located in the upper reaches of the Heihe River Basin, which encompasses ~13% of the Qilian Mountains region. We furthermore document that 82% of the HT was initiated in the last 10 years. The thermokarst terrain is observed primarily in areas with shallow active layer depth, on northern shaded slopes of 3–25°, with low solar radiation and moderate elevations ranging from 3200 to 4000 m. This first inventory of HT features is an important and missing piece in documenting changes on the Qinghai-Tibetan Plateau, and this new dataset also provides an important basis for further studies on, e.g., quantitative assessment losses caused by HT. The datasets are available from the National Tibetan Plateau/Third Pole Environment Data Center and can be downloaded from https://doi.org/10.11888/Cryos.tpdc.300805 (Peng and Yang, 2023).

1 Introduction

The Qilian Mountains are located in the northeastern part of the Qinghai-Tibetan Plateau, at the confluence of three major geographical regions that include the eastern monsoon zone, the northwestern arid zone, and the alpine zone of the Qinghai-Tibetan Plateau. The Qilian Mountains play an important role in maintaining the ecological balance of the Tibetan Plateau, stopping the southward progression of deserts, and maintaining the stability of the oases in the Hexi Corridor. Due to its unique geographical and environmental characteristics, permafrost is widespread and underlies about 50% of the area (Ran et al., 2021a). Permafrost has an important role instoring frozen water, thereby contributing to water conservation (Wang et al., 2022). These roles can aid in inland river runoff recharge, which is crucial to regional ecology, production, and life. Due to climate warming and human activities, significant permafrost degradation results in the frequent occurrence of thermokarst, representing a serious threat to ecological security and adversely impacts the environment and human beings.

Despite the importance of thermokarst processes and their potential geohazards, the distribution of thermokarst landscapes is currently mostly undocumented. The available distribution of thermokarst in the Northern Hemisphere, including retrogressive thaw slumps (RTSs), thermokarst lakes, and other terrain features, represents mainly probabilistic estimates (Olefeldt et al., 2016). Muster et al. (2017) determined the distribution of circumpolar Arctic permafrost lakes and ponds from 2002-2013 at a resolution of 5 m using optical remote sensing, satellite (Geo-Eye, QuickBird, WorldView-1 and -2, KOMPSAT-2), and radar imagery (TerraSAR-X), but temporal inconsistencies make comparisons in time and space difficult. At the regional scale, the techniques and spatial resolution of remote sensing imagery currently used at different study areas are inconsistent, e.g., estimating the distribution and development of RTSs on Banks Island, Canada, based on the interpretation of Google Earth satellite images (Lewkowicz & Way, 2019). Satellite imagery at 30-m resolution from Landsat has been used to analyze RTSs and thermokarst lakes in circumpolar Alaska, eastern Canada, and Siberia (Nitze et al., 2018). The permafrost zone of the Qinghai-Tibetan Plateau (QTP) has been a site of thermokarst geomorphology research in recent years. For example, combining field surveys and SPOT-5 satellite data for August 2010, a total of 2,163 thermokarst lakes and ponds were recorded within 10 km on either side of the Chumar River to Fenghuo Mountain of the Qinghai-Tibet Railway, with a total surface area of 1.09×10^7 m^2 and ranging in size from 100 m^2 to 4.49×10^5 m^2 (Luo et al., 2015; Niu et al., 2014). In the Beiluhe region of the central QTP, the number of RTSs increased from 124 to 438 between 2008 and 2017, with an approximate 9-fold increase in area (Huang et al., 2020; Luo et al., 2019). The latest results show that the number of RTSs on the QTP is 2669, but for the Qilian Mountains in the northeastern part of the region, only 6 (Luo et al., 2022) or as many as 15 are documented (Mu et al., 2020). A lack of a thermokarst inventory in this region is therefore evident, representing a crucial gap in the RTSs inventory on the QTP.

The Qilian Mountains impact the ecology of the QTP where permafrost degradation causes frequent freeze/thaw-induced hazards. The ecological environment of the permafrost areas has a significant impact, and there is a direct correlation between human activities and major permafrost engineering problems, including uneven subsidence of infrastructure, slumps, and cracks. Meanwhile, there is little to no information regarding hillslope thermokarst (HT) features such as RTSs, active-layer detachment slides, and thermal erosion gullies in the region (Gooseff et

Earth System
Science
Data

90 al., 2009). Thus, the urgent need to survey and quantify these undocumented terrain
91 features in the Qilian Mountains motivates and represents the goal of this study.
92

2 Study Area

94 The Qilian Mountains are located at the northern edge of the QTP, with an
95 average elevation of 3855 m. The region is underlain by permafrost and seasonally
96 frozen ground (36-40°N and 94-104°E, Figure 1a), with a permafrost area of 94,235
97 km^2 that accounts for 49% of the study domain. Characterized by both an alpine
98 mountain climate and a temperate continental monsoon climate, the mean annual air
99 temperature is 0.30°C (Jin et al., 2022) with high precipitation variability and higher
100 amounts in the southeast during the thawing season of June to September (Chen et al.,
101 2013). Due to human activities, climate change, and earthquakes, permafrost
102 instability in Qilian Mountains has gradually increased, resulting in HT formation
103 including RTSs, thermokarst lakes, and thermal erosion gullies, which pose a direct
104 threat to the local economy, ecology, and security.
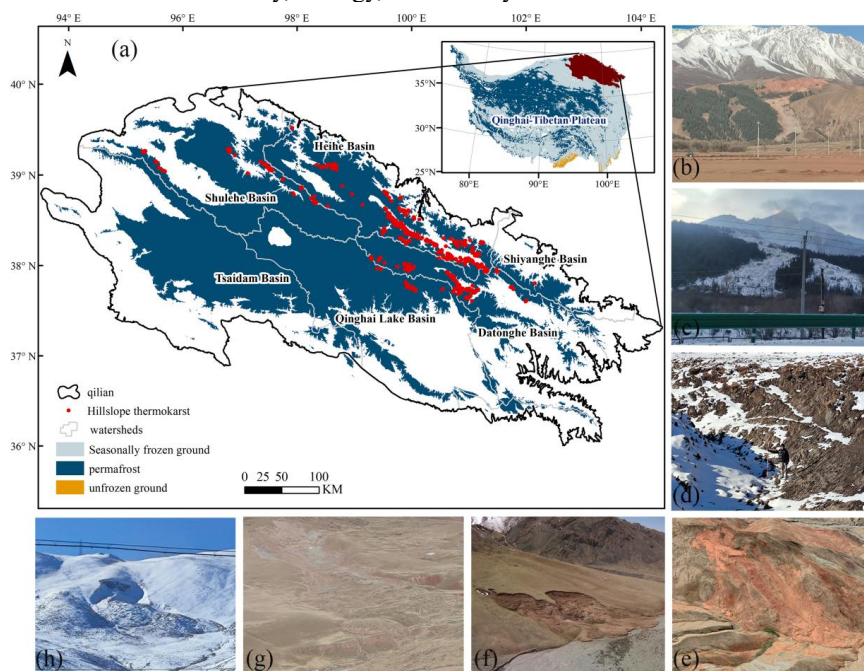
105
106 Figure 1. The location of the study area and a) its HT distribution (QTP permafrost
107 extent data are from (Zou et al., 2017) and the Qilian Mountains delineation from
108 Sheng et al., 2020), and b)–h) HT features obtained from different watersheds during
109 our field surveys with the exception of e) a © Google Earth image, as this site is too
110 difficult to access.
111

3 Data Sources

113 We collected and collated validated satellite imagery available starting in 1999 for
114 temporal detection of the onset of the HT formation. These data include unmanned
115 aerial vehicle imagery (e.g., Figure 1b–h) and 30 m resolution digital elevation model
116 data from the Shuttle Radar Topography Mission (Farr et al., 2007). A combination of
117 Omap and Google Earth software was used to detect the location of HT occurrence,

118 and Wayback imagery provided by ESRI was used to access high-resolution (<1 m)
119 satellite imagery to aid in the identification (Table 1). In addition, we used digital
120 elevation model data to tabulate variables such as slope and topographic position
121 index (TPI) of the HT. The TPI is calculated as follows:

122
$$\text{TPI} = \log_{10}\left(\frac{E}{Mean\,E} + 1\right) \times \left(\frac{S}{Mean\,S} + 1\right) \tag{1}$$

123 where E is the elevation (m), S is the slope (°), and $Mean$ indicates that the mean
124 value for the region of interest.
125   To further analyze the distribution of HT and the analogous environmental
126 variables, we apply mean annual ground temperature (MAGT) and permafrost types
127 from Ran et al. (2018). Permafrost types are divided into six MAGT categories: very
128 stable (MAGT<-5.0°C), stable (-5.0°C<MAGT<-3.0°C), semi-stable
129 (-3.0°C<MAGT<-1.5°C), transitional (-1.5°C<MAGT<-0.5°C), unstable
130 (-0.5°C<MAGT<0°C), and very unstable (MAGT>0°C) (Ran et al., 2021b). We also
131 obtain seismic data from the U.S. Geological Survey
132 (https://earthquake.usgs.gov/earthquakes/search/) describing earthquakes, including
133 their timing, epicenter location, and magnitude. To categorize vegetation types into
134 deciduous-coniferous forests (DCF), undergrowth (U), alpine scrub meadow (ASM),
135 alpine meadow (AM), alpine grassland (AG), alpine vegetation (AV), and
136 non-vegetated area (NA), based on data from the Resource and Environment Science
137 and Data Center (https://www.resdc.cn/data.aspx?DATAID=122). To assess the
138 relationship of air temperature and precipitation with HT, we download monthly 2 m
139 mean air temperature and precipitation from the fifth generation of the European
140 Centre for Medium-Range Weather Forecasts (ECMWF) reanalysis (ERA5;
141 https://cds.climate.copernicus.eu/cdsapp#!/dataset/reanalysis-era5-land-monthly-mean
142 s?tab=overview).
143

144
145
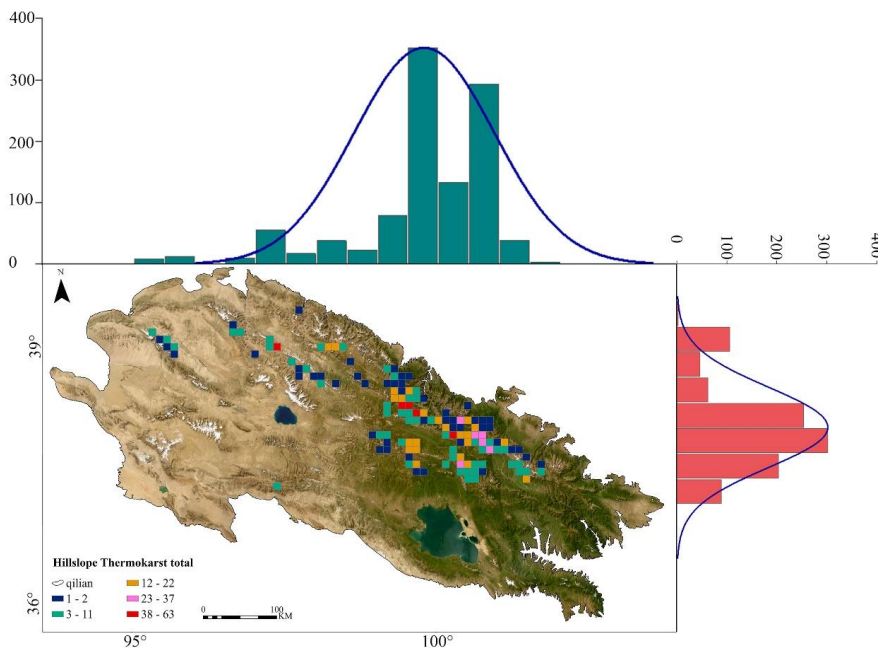
Figure 2. Frequency distribution of HT on the Qilian Mountains. The concentration of HTs is shown per 100 km^2 grid cell, with the histograms denoting the latitudinal (red) and longitudinal (green) distributions of HT and their curve fits (blue).

4 Methods

4.1 Manual Mapping

We first quantified and mapped HT via remote sensing observations. Most occurrences of HT in the permafrost region of the Qilian Mountains since 2000 were compiled by visual interpretation in Google Earth Pro and Omap. They were also aided by high resolution (<1 m) observations from Esri Wayback Imagery, which archives all published versions of world imagery (Table 1). We used a fishnet with a mesh size of 1×1 km to segment the latest satellite imagery for the entire Qilian Mountains to quantify HT mesh by mesh. RTSs are often horseshoe shaped, tongue shaped, elongated, branched, and circle chair-shaped (Lantuit & Pollard, 2008; Yin et al., 2021), characterized by a headwall, collapsed layer, and accumulation area (Lantz & Kokelj, 2008). These features are tonally and morphologically different from thermokarst landslides and their surroundings in color satellite images during the thawing season. Landslides also produce folded textures due to accumulation, which appear as laterally folded stripes on imagery. Active-layer detachment slides are a common shallow landslide in permafrost areas. Their destabilization characteristics vary depending on vegetation cover, slope, and permafrost conditions, but common features are highly disturbed slopes and lateral shear zones, as well as fracture zones formed after active layer slippage (Lewkowicz, 2007).We detected and sketched these features based on morphological, tonal, textural, shading, and other characteristics on remote sensing images, and then digitized their morphological features into polygonal data. Although the accuracy of this type of visual interpretation is relatively high, some HT features can be missed via this manual interpretation. To reduce such errors, satellite images of the similar period from different sources were evaluated four times using the same methods to ensure accurate results. The date of the satellite image when perturbations caused by HT can be first observed was defined as the initiation year of a particular HT feature. Depending on the initiation year, HT is categorized as occurring before 2010, 2010–2015, or after 2015. To observe the temporal evolution of HT features, we used the initiation year and retraced historical images covering the Qilian Mountains, a process that also helped us distinguish between HT features and one-time transient landslides.

4.2 Field Verification

Similar HT can have different morphological characteristics due to different triggers. It is thus difficult to identify the type of HT simply through imagery. In addition, after an initial trigger and HT formation, thermokarst can evolve into different types. For example, active layer detachment slides may transition into RTS due to the exposure of subsurface ice at the trailing edge and water erosion due to melting, which can cause the RTS to further progress into mudflows. Therefore, with visual interpretation based on imagery only providing individual snapshots, it is essential to also conduct field surveys as al validation exercise. We conducted a total of three field surveys in winter 2022, and spring and summer of 2023. Field work covered the Shiyanghe basin, Heihe basin, Datonghe-Huangshui basin, Qinghai Lake basin, and Shulehe basin. Due to the harsh climatic conditions and accessibility issues in the Qilian Mountains, unmanned aerial vehicles were used to survey and verify hard-to-reach areas.

196

197 Table 1. List of the data used for manual interpretation and mapping for HTs

Software Platform	Time Span	Resolution	Data Sources
Google Earth pro	1999-2022	0.6 m	Quickbird, IKONOS, SPOT-5
Omap	since 2021	<1 m	GF-2
ESRI World Imagery	since 2014	<1 m	Esri Wayback Imagery
UAV images	Feb., Apr., May 2023	~15 cm	Field Surveys

198

199 *4.3 Morphological and Spatial Statistical Analysis*

200 A landscape shape index (LSI) can be quantified to characterize shape complexity
201 by calculating the degree of deviation of a given patch from a circle or square of the
202 same area. To quantify the shape characteristics of HT features, two LSIs are
203 calculated as follows:

$$LSI_{square} = \frac{0.25P}{\sqrt{A}} \qquad (2)$$

$$LSI_{round} = \frac{P}{2\sqrt{\pi A}} \qquad (3)$$

206 where P is the perimeter (m) and A is the area (m^2). The closer the values of LSI_{square}
207 or LSI_{round} are to 1, the more square or round the shape of the HT feature is,
208 respectively.

209 To further investigate the spatial distribution of HT, we computed a global
210 Moran's index, z-score and p-value to determine whether there is autocorrelation in
211 the spatial distribution of HT. Where p-value and z-score are used to measure
212 statistical significance, when p-value < 0.01 and z-score > 2.58, it means that there is
213 a 99% probability that the elements are clustered within the study area, and the
214 smaller the p-value and the larger the z-score, the greater the probability that such
215 spatial patterns are clustered. Moran's index ranges from -1 to 1, with negative values
216 meaning negative correlation, positive values meaning positive correlation, and 0
217 denotes that the spatial objects in the study area are independent of each other.
218 Additionally, the closer the index is to 1, the more clustered the HT features are, and
219 the closer of the index is to -1, the more dispersed the HT features are. To delineate
220 the regions that may have spatial autocorrelation (Bivand & Wong, 2018), we further
221 process local autocorrelation on this basis. The local autocorrelation regions are
222 divided into four types: high-high (HH) clustering, high-low (HL) clustering,
223 low-high (LH) clustering, and low-low (LL) clustering, based on the local Moran's
224 index. HH represents a higher amount of HT and a higher amount of HT in the
225 neighboring region; HL represents a higher amount of HT and a lower amount of HT
226 in the neighboring region; LH represents a lower amount of HT and a higher amount
227 of HT in the neighboring region; and LL represents a lower amount of HT and a lower
228 amount of HT in the neighboring region. Although the methods described above can
229 identify global and local spatial autocorrelation, respectively, they are unable to
230 identify clusters of concentrated HT features. We therefore also apply hot spot
231 analysis, which is another effective way of exploring the characteristics of local
232 spatial distributions. All the above techniques are based on spatial statistical analysis
233 functions of ArcGIS.

234 To determine the effects of climate on HT, we average 2-m air temperature and
235 precipitation from ERA5 over the period 2000–2020 and calculate their standard
236 deviations (Figure 6).
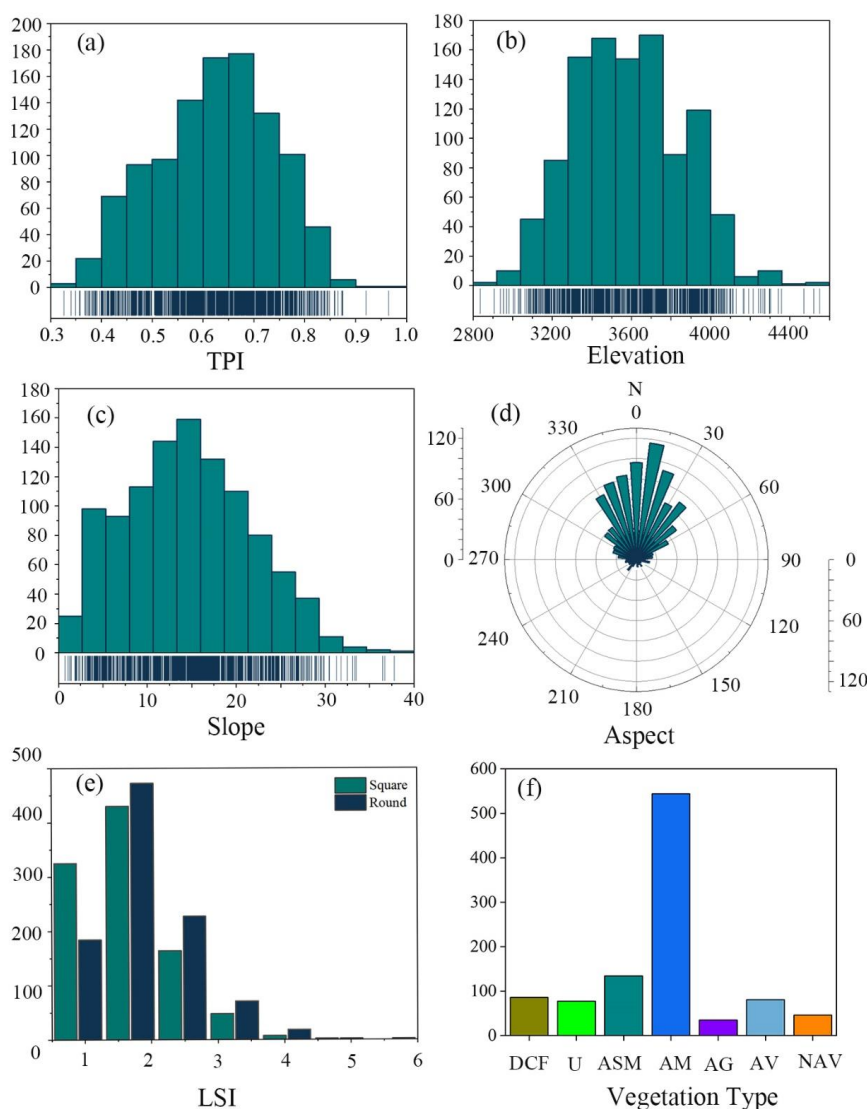
Figure 3. The number of HT terrain features (y-axes) of HT as categorized by (a) topographic position index (TPI), (b) elevation, (c) slope , (d) aspect, (e) landscape shape index (LSI), and (f) vegetation type including deciduous coniferous forests (DCF), undergrowth (U), alpine scrub meadow (ASM), alpine meadow (AM), alpine grassland (AG), alpine vegetation (AV), and non-vegetated area (NA); the blue vertical lines at the bottom of panels a–c represent the number of HT features in each x-axis bin.

5 Results

247   Our inventory of HT includes the Heihe Basin, Shulehe Basin, Datonghe Basin,
248   Shiyanghe Basin, Qinghai Lake Basin, and Tsaidam Basin within the Qilian
249   Mountains, with a total of 1064 HT features. In any 100 km^2 grid cell, the maximum
250   density of HT is 63 (Figure 2).This density is lower than the 68 per 25 km^2 in the
251   central Tibetan Plateau reported by Luo et al. (2022) and 88 per 25 square km^2 on
252   Banks Island, Canada from Lewkowicz & Way (2019). 67% of these HT features
253   were identified in the Heihe River basin, followed by the Datong River Basin,
254   accounting for 19%. The HT distribution in these river basins is irregular,
255   corroborated by a positive statistically significant Moran's index value of 0.3, p-value
256   of 0.00001 and z-score of 32.5. Of all the HT features, the largest is 58 ha, the
257   smallest area is 0.01 ha, with most being smaller than 10 ha. The average area is 1.75
258   ha, with a total area of 1708 ha.
259   The spatial distribution of HT on the QTP is strongly controlled by terrain factors
260   such as the elevation, slope, TPI, and aspect (Luo et al., 2022). The statistical results
261   indicate that HT is observed at elevations ranging from 2,835 to 4,550 m. However,
262   90% of RTSs are more likely to occur at elevations ranging from 3,200 to 4,000 m in
263   the middle/high elevation area of the Qilian Mountains. HT tends to occur on
264   north-facing slopes (Figure 3b and 3d), with slopes ranging from 3° to 25° (Figure 3c).
265   In addition, the TPI shows that ~85% of the HTs occur mainly between 0.5 and 0.8
266   (Figure 3a), suggesting that they commonly occur in locations that are lower than their
267   surroundings. Both LSI indices suggest that 75% of HT has values close to 1.0
268   (Figure 3e), indicating that most HT is simple in shape and compact in morphology,
269   rather than elongated (Niu et al., 2016), implying it has a relatively low probability of
270   being reactivated (Yang et al., 2023). Alpine meadow areas contain ~53% of HT,
271   followed by alpine scrub meadows, which contain 13% (Figure 3f).
272   The initiation years of HT features are variable across the study area. 187 HT
273   features (18%) were identified before 2010, and the remaining 82% in the last 10
274   years. 392 sites (37%) were initiated in 2010-2015 and 482 (45%) after 2015. Much
275   of the newly initiated HT occurred in the middle and upper reaches of the Datonghe
276   basin bordering the Heihe basin (Figure 4), which is also a HT hotspot region. The
277   recent increase in HT can be attributed to the anomalous weather conditions in the
278   corresponding years. The association between newly observed HT and meteorological
279   data indicates a sudden HT increase in years with unusually high temperatures during
280   the thawing season (Figure 6).

281
282 Figure 4. The timing of HT initiation within 100 km² grid cells.
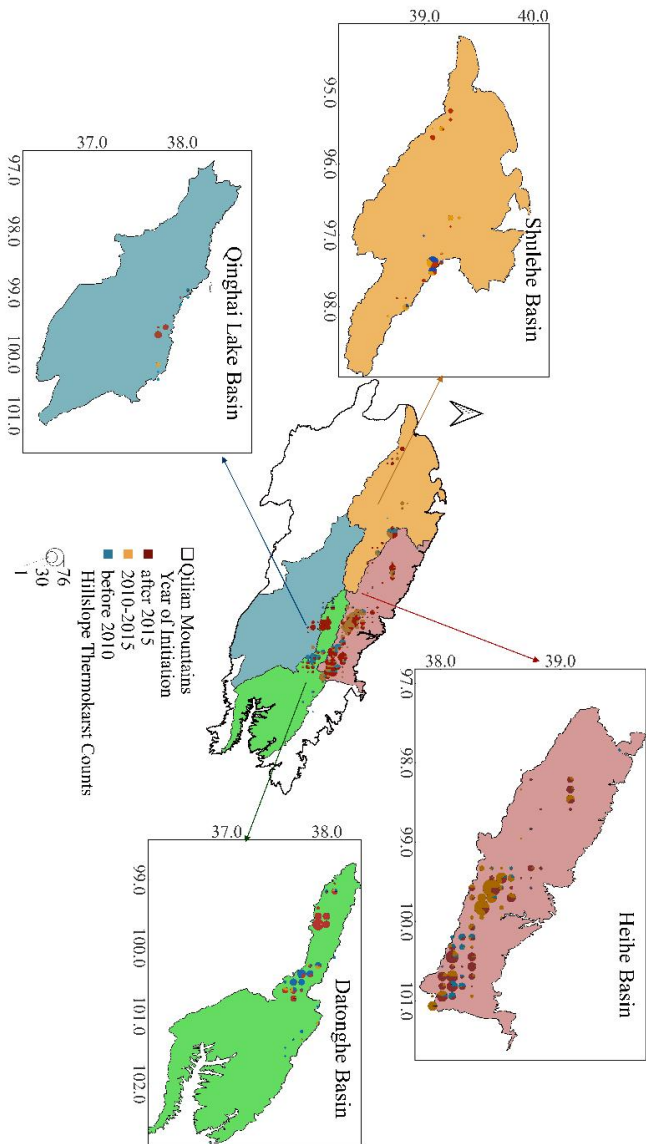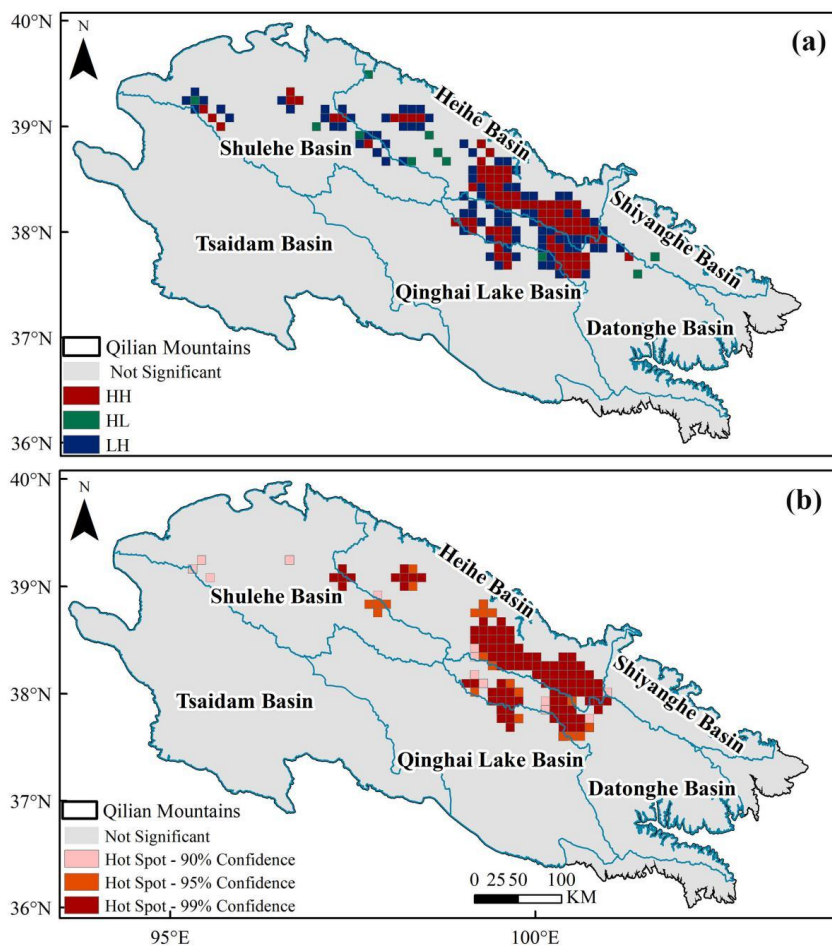
Figure 5. (a) Spatial auto-correlation indicating high-high (HH), high-low (HL), and low-high (LH) clustering, and (b) hotspot analysis where the different colors represent the confidence levels.

6 Discussion

6.1 Drivers of HT in the Qilian Mountainous

6.1.1 Permafrost Conditions

Formation of HT is facilitated by thick subsurface ice and various internal and external environmental conditions (Stephani et al., 2023). Permafrost stability in ~80% of the permafrost area of the Qilian Mountains is predominantly transitional, and higher permafrost temperatures (Ran et al., 2021a) will exacerbate the climate sensitivity of this area (Lewkowicz & Way, 2019; Patton et al., 2021) leading to melting of the subsurface ice and an increase in active layer thickness, thus decreasing the stability of the slope (Behnia & Blais-Stevens, 2018). This is also supported by our finding that ~90% of HT occurs in the transition zone between permafrost and seasonally frozen soil where mean annual ground temperature is greater than -1°C.

6.1.2 Environmental Factors

301
302   Topographic conditions facilitate the formation of subsurface ice and the
303 continuous development of HT. At elevations below 5100 m on the QTP, aspect
304 dominates the distribution of permafrost. More permafrost underlies regions of shaded,
305 north-facing slopes than sunny south-facing slopes (Ran et al., 2021a). Indeed, we
306 find that ~95% of Qilian Mountain HT is found on north-facing slopes where it also
307 enhances vegetation growth and soil moisture storage (Jin et al., 2009). Lower solar
308 radiation, higher permafrost ice content, and shallow active layer thickness (Lacelle et
309 al., 2015; Ward Jones et al., 2019) also enables HT formation (Luo et al., 2022; Niu et
310 al., 2016; Xia et al., 2022). We find more than half of the HT occurs in alpine
311 meadows, which require more water content than alpine steppes (Yin et al., 2017) and
312 consequently also results in more ground ice development under this vegetation type.
313 We determined that ~90% of HT in the Qilian Mountains occurs on 3° to 25° slopes.
314 Low and gentle slopes are favorable for groundwater pooling (Luo et al., 2022),
315 whereas slopes greater than 16° are relatively steep and therefore not conducive to
316 groundwater enrichment for ice formation, but such slopes also provide dynamic
317 conditions for active layer detachments and collapsing ground (Wang, 1990). We also
318 observe more HT initiation at locations that are lower compared to their surroundings,
319 as such depressions favor the accumulation of snow and rainwater (Stieglitz et al.,
320 2003) and prevent heat loss from the soil. This encourages melting of subsurface ice
321 (Zhang, 2005) at the base of the active layer and, after an unstable layer is formed
322 between the permafrost and the active layer, the overlying soil can slide along the
323 slope (Patton et al., 2021).

324   The Qilian Mountains were and are still formed by the ongoing collision of the
325 Indian Ocean Plate and the Eurasian Plate, resulting in the Qilian Mountains-Hexi
326 Corridor active fault system (Xiong et al., 2017) that has seen nearly 400 earthquakes
327 of magnitude 2 or greater over the past two decades. In particular, the high seismic
328 activity of the Heihe, Shiyanghe, and Datonghe Basins (Figure 7a) represents a
329 potential threat to the safety and integrity of current and future infrastructure in the
330 region. During our field investigations we found a nearly 3 km long and 2 m deep
331 slope fracture caused by a 6.9-magnitude earthquake in 2022, resulting in a massive
332 exposure of subsurface ice and the collapse of the Lanzhou-Xinjiang High Speed Rail
333 Tunnel (Figure 7b and c). The occurrence of an earthquake can result in an
334 instantaneous increase in pore water pressure and slope sliding forces that reduce
335 slope stability and potentially leads to a massive exposure of subsurface ice (Niu et al.,
336 2016), sediment liquefaction (Dadfar et al., 2017), and permafrost warming (Che et al.,
337 2014), creating the ideal setting for active-layer detachment slides.

338

6.1.3 Climate Factors

339
340   Extreme summer temperatures and precipitation have been identified as triggers
341 for the initiation of RTSs in many Arctic permafrost zones (Balser et al., 2014; Kokelj
342 et al., 2015; Lewkowicz & Way, 2019; Segal et al., 2016). Given our finding that 82%
343 of HT was initiated in the last decade (Figure 4), mostly during 2010-2015 and after
344 2015, we used ERA5 to determine the temperature and precipitation characteristics
345 for the Qilian Mountains over the last 20 years (Li et al., 2022) (Figure 6, the square
346 symbols). The mean thawing season air temperatures in 2010 and 2016 were higher
347 than in other years (Figure 6a, red square symbols). A warming thaw season could
348 lead to thaw consolidation at the base of the active layer or to higher porewater
349 pressure in the transient thaw layer, reducing the effective shear strength, and causing
350 slope failure (Lewkowicz & Way, 2019). The anomalous air temperatures during the

351 thawing season could accelerate permafrost thaw and expose ice-rich permafrost, thus
352 leading to new HT (Figure 6a, dark brown and dark red bars,respectively). Rainfall
353 infiltration may transfer heat to the top layer of permafrost and induce melting of
354 ground ice in ice-rich transient layers, which would increase the porewater pressure at
355 the active layer-permafrost interface and thereby trigger formation of HT (Luo et al.,
356 2022). However, precipitation variability during the thawing season does not match
357 HT formation (Figure 6b). Despite high precipitation in both 2007 and 2018 (Figure
358 6b, blue square symbols), no initiation of HTwas found to subsequently coincide with
359 these peaks, and precipitation also does not explain the significant initiation of HTs
360 between 2010-2015, nor after 2015 (Figure 6b, yellow and red bars, respectively). The
361 same conclusion also applies to the other three sub-regions—Hoh Xil Mountain,
362 Maqu country, and Honglianghe—and it could be speculated that the nature of the
363 soils on the QTP may instead play a role (Luo et al., 2022).
364
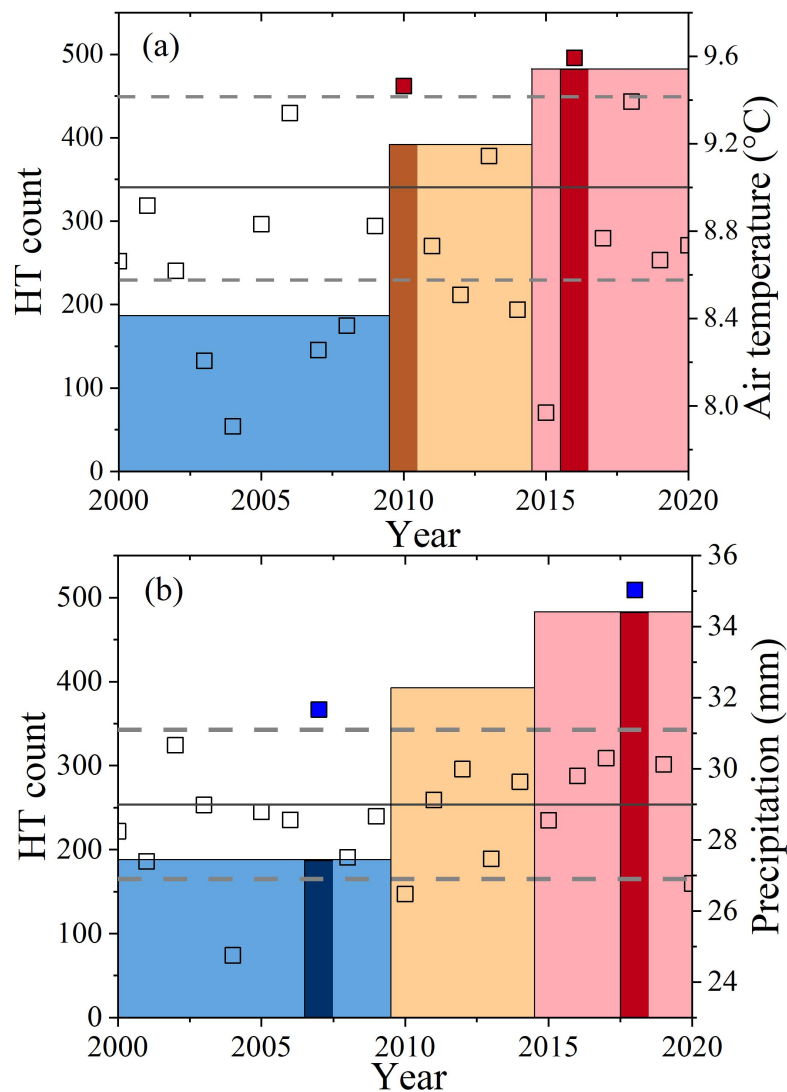
366 Figure 6. The relationship between HT numbers (unequal width bars, the darker colors
367 represent years with extreme weather events.) and (a) temperature and (b)
368 precipitation in the thawing season from 2000 to 2020 (square symbols, the red
369 squares and the blue squares represent the extreme weather events.). The solid
370 horizontal line represents the mean, and the dashed line represents ±1 standard
371 deviation.
372

6.1.4 Human Activities

374   Extensive and increasing human activities have been shown to significantly
375 accelerate permafrost degradation (Cheng & Jin, 2013; IPCC, 2019). The total
376 population of the Qilian Mountains is about 60,000, there are approximately 1,000
377 metal, energy, and other types of mineral deposits (National Mineral Properties

378   Database 2021 Edition, http://data.ngac.org.cn/mineralresource/index.html), and there
379   are ~8,000 km of railroads and highways. The core of this human activity is
380   concentrated on the eastern side of the Qilian Mountains, which generally coincides
381   with the spatial distribution of the HT hotspots we documented. This qualitatively
382   suggests a role of human activities on HT from, e.g., engineering disturbances,
383   vegetation degradation due to overgrazing, etc. (Sharkhuu et al., 2007). Establishing
384   the impact of human activities on HT quantitatively is still a difficult challenge, but
385   our identification of the location and timing of HT formation is a first, important step
386   for further future studies, especially on the socioeconomic development in the region.
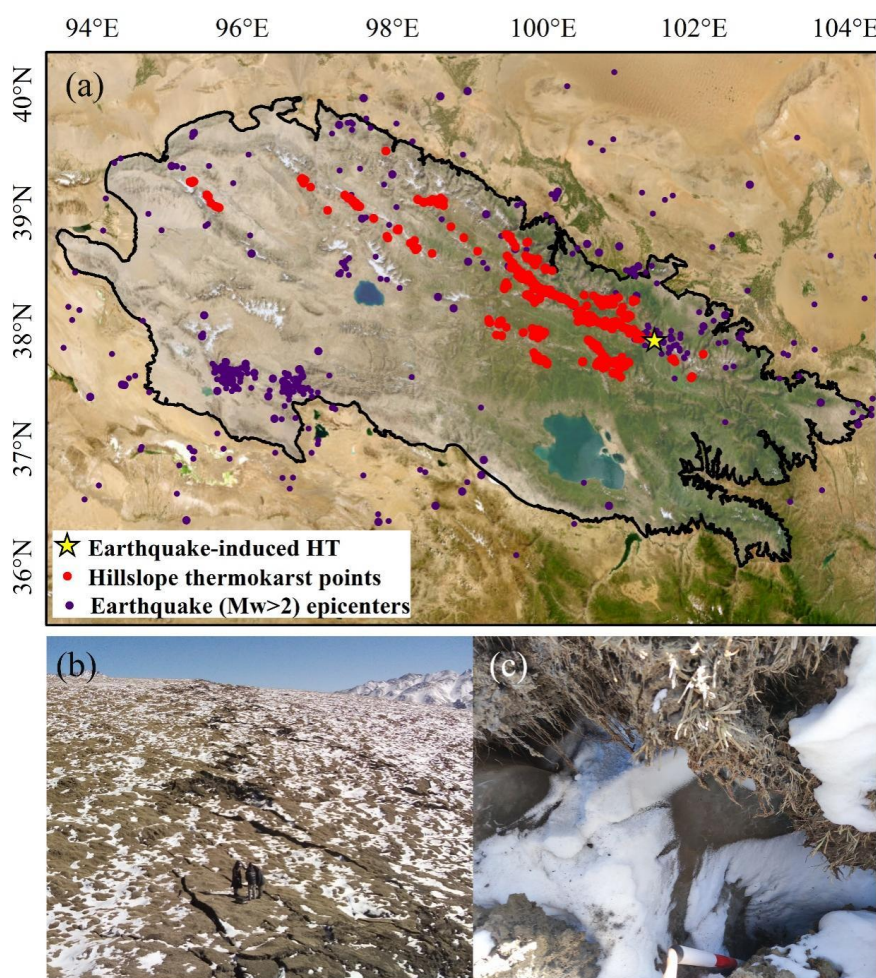
387
388   Figure 7. Qilian Mountains showing (a) the location of HT locations and earthquakes
389   with magnitude >2 in the last 20 years, (b) slope fractures caused by earthquakes, and
390   (c) exposed subsurface ice.
391
392
393   **7 Data Availability**
394

395 DEM data can be accessed through NASA
396 (https://www.earthdata.nasa.gov/sensors/srtm). Landsat5-8 data are available from
397 USGS (https://www.usgs.gov/) and Sentinel-2 from ESA (https://www.esa.int/), and
398 can be downloaded through Google Earth Engine. Esri World Imagery can be
399 accessed through Esri Wayback Imagery at: https://livingalas.arcgis.com. Some GF-2
400 imagery is also available online through Omap software, and high resolution 3D
401 satellite imagery of the Qilian Mountain region can be viewed in Google Earth
402 software. High-resolution satellite images captured by the Jilin-1 satellite in China can
403 be viewed by accessing https://www.jl1mall.com/rskit/. The HT inventory for the
404 Qilian Mountains can be freely downloaded from the National Tibetan Plateau/Third
405 Pole Environment Data Center (https://doi.org/10.11888/Cryos.tpdc.300805, Peng and
406 Yang, 2023).
407

408 **8 Conclusion**
409 This study used visual interpretation and field investigations for repeated verification
410 to investigate HT in the permafrost zone of the Qilian Mountains. We successfully
411 produced the first HT inventory for this area, and found it contains a total of 1064 HT
412 features. The area of these features ranged from 0.01 to 58 ha, with an average of 1.75
413 ha. Thermokarst is primarily concentrated at the junction between the upstream
414 portion of the Heihe River Basin and the mid- and upstream portion of the Datonghe
415 Basin. Within a 10×10 km area, thermokarst has a maximum density of 63 features,
416 affecting an area of ~20 km^2. HT in the Qilian Mountains is more likely to occur on
417 north-facing shaded slopes, at elevations between 3200–4000 m, slopes of 3–25°,
418 0.5<TPI<0.8, and in alpine meadow vegetation. Based on long-term satellite imagery,
419 874 new HT features were initiated after 2010, accounting for 82% of the total HT.
420 Recent higher air temperatures during the thawing season are likely important reasons
421 for the intensification of HT formation in the Qilian Mountains, while precipitation
422 does not seem to play a role. This first HT inventory for the Qilian Mountains will be
423 fundamental for quantitative assessments that explore the exact causes and underlying
424 thermokarst processes, and ultimately allow for better identification prediction of
425 areas prone to thermokarst formation in the future.
426

427 **Author contributions.** XP and GY designed the research and obtained funding. GY
428 analyzed the data and prepared the data files. GY, WT, XL and XP conducted the field
429 work. GY, XP, OWF, JL, CM, FN wrote the paper with input from the coauthors and
430 coordinated the analysis and contributions from all coauthors. XP and GY contributed
431 to the work equally and should be regarded as co-first authors.
432

433 **Competing interests.** The contact author has declared that neither they nor their
434 coauthors have any competing interests.
435

436 **Disclaimer.** Publisher's note: Copernicus Publications remains neutral with regard to
437 jurisdictional claims in published maps and institutional affiliations.
438

439 **Acknowledgements**
440 This work was supported by the Second Tibetan Plateau Scientific Expedition and
441 Research Program (STEP) (2019QZKK0905), the National Natural Science
442 Foundation of China (42161160328, 42171120), and the Fundamental Research Funds
443 for the Central Universities (lzujbky-2023-01).
444

References

Balser, A. W., Jones, J. B., and Gens, R.: Timing of retrogressive thaw slump initiation in the Noatak Basin, northwest Alaska, USA, J. Geophys. Res. Earth Surf., 119, 1106–1120, https://doi.org/10.1002/2013JF002889, 2014.

Behnia, P. and Blais-Stevens, A.: Landslide susceptibility modelling using the quantitative random forest method along the northern portion of the Yukon Alaska Highway Corridor, Canada, Nat. Hazards, 90, 1407–1426, https://doi.org/10.1007/s11069-017-3104-z, 2018.

Bivand, R. S. and Wong, D. W. S.: Comparing implementations of global and local indicators of spatial association, TEST, 27, 716–748, https://doi.org/10.1007/s11749-018-0599-x, 2018.

Che, A., Wu, Z., and Wang, P.: Stability of pile foundations base on warming effects on the permafrost under earthquake motions, Soils Found., 54, 639–647, https://doi.org/10.1016/j.sandf.2014.06.006, 2014.

Chen, H., Zhu, Q., Peng, C., Wu, N., Wang, Y., Fang, X., Gao, Y., Zhu, D., Yang, G., Tian, J., Kang, X., Piao, S., Ouyang, H., Xiang, W., Luo, Z., Jiang, H., Song, X., Zhang, Y., Yu, G., Zhao, X., Gong, P., Yao, T., and Wu, J.: The impacts of climate change and human activities on biogeochemical cycles on the Qinghai-Tibetan Plateau, Glob. Change Biol., 19, 2940–2955, https://doi.org/10.1111/gcb.12277, 2013.

Cheng, G. and Jin, H.: Permafrost and groundwater on the Qinghai-Tibet Plateau and in northeast China, Hydrogeol. J., 21, 5–23, https://doi.org/10.1007/s10040-012-0927-2, 2013.

Dadfar, B., El Naggar, M. H., and Nastev, M.: Quantifying exposure of linear infrastructures to earthquake-triggered transverse landslides in permafrost thawing slopes, Can. Geotech. J., 54, 1002–1012, https://doi.org/10.1139/cgj-2017-0076, 2017.

Farr, T. G., Rosen, P. A., Caro, E., Crippen, R., Duren, R., Hensley, S., Kobrick, M., Paller, M., Rodriguez, E., Roth, L., Seal, D., Shaffer, S., Shimada, J., Umland, J., Werner, M., Oskin, M., Burbank, D., and Alsdorf, D.: The Shuttle Radar Topography Mission, Rev. Geophys., 45, https://doi.org/10.1029/2005RG000183, 2007.

Gooseff, M. N., Balser, A., Bowden, W. B., and Jones, J. B.: Effects of Hillslope Thermokarst in Northern Alaska, Eos Trans. Am. Geophys. Union, 90, 29–30, https://doi.org/10.1029/2009EO040001, 2009.

Huang, L., Luo, J., Lin, Z., Niu, F., and Liu, L.: Using deep learning to map retrogressive thaw slumps in the Beiluhe region (Tibetan Plateau) from CubeSat images, Remote Sens. Environ., 237, 111534, https://doi.org/10.1016/j.rse.2019.111534, 2020.

Jin, H., Li, X., Frauenfeld, O. W., Zhao, Y., Chen, C., Du, R., Du, J., and Peng, X.: Comparisons of statistical downscaling methods for air temperature over the Qilian Mountains, Theor. Appl. Climatol., 149, 893–896, https://doi.org/10.1007/s00704-022-04081-w, 2022.

485 Jin, X., Wan, L., Zhang, Y.-K., Hu, G., Schaepman, M. E., Clevers, J. G. P. W., and Su,
486 Z. B.: Quantification of spatial distribution of vegetation in the Qilian Mountain area
487 with MODIS NDVI, Int. J. Remote Sens., 30, 5751–5766,
488 https://doi.org/10.1080/01431160902736635, 2009.

489 Kokelj, S. V., Tunnicliffe, J., Lacelle, D., Lantz, T. C., Chin, K. S., and Fraser, R.:
490 Increased precipitation drives mega slump development and destabilization of ice-rich
491 permafrost terrain, northwestern Canada, Glob. Planet. Change, 129, 56–68,
492 https://doi.org/10.1016/j.gloplacha.2015.02.008, 2015.

493 Lacelle, D., Brooker, A., Fraser, R. H., and Kokelj, S. V.: Distribution and growth of
494 thaw slumps in the Richardson Mountains–Peel Plateau region, northwestern Canada,
495 Geomorphology, 235, 40–51, https://doi.org/10.1016/j.geomorph.2015.01.024, 2015.

496 Lantuit, H. and Pollard, W. H.: Fifty years of coastal erosion and retrogressive thaw
497 slump activity on Herschel Island, southern Beaufort Sea, Yukon Territory, Canada,
498 Geomorphology, 95, 84–102, https://doi.org/10.1016/j.geomorph.2006.07.040, 2008.

499 Lantz, T. C. and Kokelj, S. V.: Increasing rates of retrogressive thaw slump activity in
500 the Mackenzie Delta region, N.W.T., Canada, Geophys. Res. Lett., 35, L06502,
501 https://doi.org/10.1029/2007GL032433, 2008.

502 Lewkowicz, A. G.: Dynamics of active-layer detachment failures, Fosheim Peninsula,
503 Ellesmere Island, Nunavut, Canada, Permafr. Periglac. Process., 18, 89–103,
504 https://doi.org/10.1002/ppp.578, 2007.

505 Lewkowicz, A. G. and Way, R. G.: Extremes of summer climate trigger thousands of
506 thermokarst landslides in a High Arctic environment, Nat. Commun., 10, 1329,
507 https://doi.org/10.1038/s41467-019-09314-7, 2019.

508 Li, Y., Qin, X., Liu, Y., Jin, Z., Liu, J., Wang, L., and Chen, J.: Evaluation of
509 Long-Term and High-Resolution Gridded Precipitation and Temperature Products in
510 the Qilian Mountains, Qinghai–Tibet Plateau, Front. Environ. Sci., 10, 906821,
511 https://doi.org/10.3389/fenvs.2022.906821, 2022.

512 Luo, J., Niu, F., Lin, Z., Liu, M., and Yin, G.: Thermokarst lake changes between
513 1969 and 2010 in the Beilu River Basin, Qinghai–Tibet Plateau, China, Sci. Bull., 60,
514 556–564, https://doi.org/10.1007/s11434-015-0730-2, 2015.

515 Luo, J., Niu, F., Lin, Z., Liu, M., and Yin, G.: Recent acceleration of thaw slumping in
516 permafrost terrain of Qinghai-Tibet Plateau: An example from the Beiluhe Region,
517 Geomorphology, 341, 79–85, https://doi.org/10.1016/j.geomorph.2019.05.020, 2019.

518 Luo, J., Niu, F., Lin, Z., Liu, M., Yin, G., and Gao, Z.: Inventory and Frequency of
519 Retrogressive Thaw Slumps in Permafrost Region of the Qinghai–Tibet Plateau,
520 Geophys. Res. Lett., 49, https://doi.org/10.1029/2022GL099829, 2022.

521 Mu, C., Shang, J., Zhang, T., Fan, C., Wang, S., Peng, X., Zhong, W., Zhang, F., Mu,
522 M., and Jia, L.: Acceleration of thaw slump during 1997–2017 in the Qilian
523 Mountains of the northern Qinghai-Tibetan plateau, Landslides, 17, 1051–1062,
524 https://doi.org/10.1007/s10346-020-01344-3, 2020.

525 Muster, S., Roth, K., Langer, M., Lange, S., Cresto Aleina, F., Bartsch, A.,
526 Morgenstern, A., Grosse, G., Jones, B., Sannel, A. B. K., Sjöberg, Y., Günther, F.,
527 Andresen, C., Veremeeva, A., Lindgren, P. R., Bouchard, F., Lara, M. J., Fortier, D.,
528 Charbonneau, S., Virtanen, T. A., Hugelius, G., Palmtag, J., Siewert, M. B., Riley, W.
529 J., Koven, C. D., and Boike, J.: PeRL: a circum-Arctic Permafrost Region Pond and
530 Lake database, Earth Syst. Sci. Data, 9, 317–348,
531 https://doi.org/10.5194/essd-9-317-2017, 2017.

532 Nitze, I., Grosse, G., Jones, B. M., Romanovsky, V. E., and Boike, J.: Remote sensing
533 quantifies widespread abundance of permafrost region disturbances across the Arctic
534 and Subarctic, Nat. Commun., 9, 5423, https://doi.org/10.1038/s41467-018-07663-3,
535 2018.

536 Niu, F., Luo, J., Lin, Z., Liu, M., and Yin, G.: Morphological Characteristics of
537 Thermokarst Lakes along the Qinghai-Tibet Engineering Corridor, Arct. Antarct. Alp.
538 Res., 46, 963–974, https://doi.org/10.1657/1938-4246-46.4.963, 2014.

539 Niu, F., Luo, J., Lin, Z., Fang, J., and Liu, M.: Thaw-induced slope failures and
540 stability analyses in permafrost regions of the Qinghai-Tibet Plateau, China,
541 Landslides, 13, 55–65, https://doi.org/10.1007/s10346-014-0545-2, 2016.

542 Olefeldt, D., Goswami, S., Grosse, G., Hayes, D., Hugelius, G., Kuhry, P., McGuire,
543 A. D., Romanovsky, V. E., Sannel, A. B. K., Schuur, E. A. G., and Turetsky, M. R.:
544 Circumpolar distribution and carbon storage of thermokarst landscapes, Nat.
545 Commun., 7, 13043, https://doi.org/10.1038/ncomms13043, 2016.

546 Patton, A. I., Rathburn, S. L., Capps, D. M., McGrath, D., and Brown, R. A.: Ongoing
547 Landslide Deformation in Thawing Permafrost, Geophys. Res. Lett., 48,
548 https://doi.org/10.1029/2021GL092959, 2021.

549 Peng, X. and Yang, G.: The hillslope thermokarst invertory for the permafrost region
550 of the Qilian Mountains (2000-2020). National Tibetan Plateau Data Center[data set],
551 https://doi.org/10.11888/Cryos.tpdc.300805, 2023.

552 Ran, Y., Li, X., Cheng, G., Nan, Z., Che, J., Sheng, Y., Wu, Q., Jin, H., Luo, D., Tang,
553 Z., and Wu, X.: Mapping the permafrost stability on the Tibetan Plateau for
554 2005–2015, Sci. China Earth Sci., 64, 62–79,
555 https://doi.org/10.1007/s11430-020-9685-3, 2021.

556 Segal, R. A., Lantz, T. C., and Kokelj, S. V.: Acceleration of thaw slump activity in
557 glaciated landscapes of the Western Canadian Arctic, Environ. Res. Lett., 11, 034025,
558 https://doi.org/10.1088/1748-9326/11/3/034025, 2016.

559 Sharkhuu, A., Sharkhuu, N., Etzelmüller, B., Heggem, E. S. F., Nelson, F. E.,
560 Shiklomanov, N. I., Goulden, C. E., and Brown, J.: Permafrost monitoring in the
561 Hovsgol mountain region, Mongolia, J. Geophys. Res., 112, F02S06,
562 https://doi.org/10.1029/2006JF000543, 2007.

563 Stephani, E., Darrow, M. M., Kanevskiy, M., Wuttig, F., Daanen, R. P., Schwarber, J.
564 A., Doré, G., Shur, Y., Jorgenson, M. T., Croft, P., and Drage, J. S.: Hillslope erosional
565 features and permafrost dynamics along infrastructure in the Arctic Foothills, Alaska,

566   Permafr. Periglac. Process., 34, 208–228, https://doi.org/10.1002/ppp.2188, 2023.

567   Stieglitz, M., Déry, S. J., Romanovsky, V. E., and Osterkamp, T. E.: The role of snow
568   cover in the warming of arctic permafrost, Geophys. Res. Lett., 30,
569   https://doi.org/10.1029/2003GL017337, 2003.

570   Wang, R., Peng, Q., Zhang, W., Zhao, W., Liu, C., and Zhou, L.: Ecohydrological
571   Service Characteristics of Qilian Mountain Ecosystem in the Next 30 Years Based on
572   Scenario Simulation, Sustainability, 14, 1819, https://doi.org/10.3390/su14031819,
573   2022.

574   Ward Jones, M. K., Pollard, W. H., and Jones, B. M.: Rapid initialization of
575   retrogressive thaw slumps in the Canadian high Arctic and their response to climate
576   and terrain factors, Environ. Res. Lett., 14, 055006,
577   https://doi.org/10.1088/1748-9326/ab12fd, 2019.

578   Xia, Z., Huang, L., Fan, C., Jia, S., Lin, Z., Liu, L., Luo, J., Niu, F., and Zhang, T.:
579   Retrogressive thaw slumps along the Qinghai–Tibet Engineering Corridor: a
580   comprehensive inventory and their distribution characteristics, Earth Syst. Sci. Data,
581   14, 3875–3887, https://doi.org/10.5194/essd-14-3875-2022, 2022.

582   Xiong, J., Li, Y., Zhong, Y., Lu, H., Lei, J., Xin, W., Wang, L., Hu, X., and Zhang, P.:
583   Latest Pleistocene to Holocene Thrusting Recorded by a Flight of Strath Terraces in
584   the Eastern Qilian Shan, NE Tibetan Plateau, TECTONICS, 36, 2973–2986,
585   https://doi.org/10.1002/2017TC004648, 2017.

586   Yang, D., Qiu, H., Ye, B., Liu, Y., Zhang, J., and Zhu, Y.: Distribution and Recurrence
587   of Warming-Induced Retrogressive Thaw Slumps on the Central Qinghai-Tibet
588   Plateau, J. Geophys. Res. Earth Surf., 128, e2022JF007047,
589   https://doi.org/10.1029/2022JF007047, 2023.

590   Yin, G., Niu, F., Lin, Z., Luo, J., and Liu, M.: Effects of local factors and climate on
591   permafrost conditions and distribution in Beiluhe basin, Qinghai-Tibet Plateau, China,
592   Sci. Total Environ., 581–582, 472–485,
593   https://doi.org/10.1016/j.scitotenv.2016.12.155, 2017.

594   Yin, G., Luo, J., Niu, F., Lin, Z., and Liu, M.: Machine learning-based thermokarst
595   landslide susceptibility modeling across the permafrost region on the Qinghai-Tibet
596   Plateau, Landslides, 18, 2639–2649, https://doi.org/10.1007/s10346-021-01669-7,
597   2021.

598   Zhang, T.: Influence of the seasonal snow cover on the ground thermal regime: An
599   overview, Rev. Geophys., 43, https://doi.org/10.1029/2004RG000157, 2005.

600   Zou, D., Zhao, L., Sheng, Y., Chen, J., Hu, G., Wu, T., Wu, J., Xie, C., Wu, X., Pang,
601   Q., Wang, W., Du, E., Li, W., Liu, G., Li, J., Qin, Y., Qiao, Y., Wang, Z., Shi, J.,
602   and Cheng, G.: A new map of permafrost distribution on the Tibetan Plateau,

603
604